CHAPTER 2

Deformation and failure of rocks under confining pressure

A state of stress that is necessary to produce rock failure in an element can be described by the three principal stresses σ_1, σ_2, and σ_3. In this book, compressive stress is taken positive and $\sigma_1 > \sigma_2 > \sigma_3$, that is, σ_1 is the maximum principal stress, σ_2 is the intermediate principal stress, and σ_3 is the minimum principal stress. In principal coordinates, the points $(\sigma_1, \sigma_2, \sigma_3)$ representing different states of stress necessary to produce failure might form a surface

$$\sigma_1 = \mathrm{f}(\sigma_2, \sigma_3) \tag{2.1}$$

for a given material. The most fundamental problem of rock mechanics is the study of the shape of this surface for various rocks. In the next chapter, this is fully discussed.

Many experiments have been done using the so-called triaxial test, in which two principal stresses are equal, $\sigma_1 > \sigma_2 = \sigma_3 > 0$ (e.g., von Kármán, 1911; Griggs, 1936; Handin, 1966) or $\sigma_1 = \sigma_2 > \sigma_3 > 0$ (e.g., Böker, 1915). In this book, the term "conventional triaxial test" is used for such cases, and the true triaxial test is used for the general case in which $\sigma_1 \geq \sigma_2 \geq \sigma_3$. In this chapter, deformation characteristics and pressure dependence of rock strength by the conventional triaxial compression test are discussed, mainly on the basis of the author's experiments.

2.1 DEFORMATION CHARACTERISTICS

2.1.a *Experimental procedure*

First, rock specimens of various types from Japan were tested at room temperature by the conventional triaxial compression method (Mogi, 1965). The testing apparatus at Waseda University in Tokyo was used in the experiments. The schematic view of the apparatus is presented in Fig. 2.1. The test specimens were cylinders of 40 mm diameter for weaker rocks and 20 mm diameter for hard rocks, the height/diameter ratio being nearly 2.0. In this case, there is the end effect for hard rocks under low confining pressure, but the revised specimen design described in the preceding chapter was used for Westerly granite and Dunham dolomite which will be discussed later in this chapter. The specimens were jacketed with soft rubber to prevent pressure fluid from entering porous rock specimens. (Thereafter, I frequently used silicone rubber for jacketing.) The axial stress was applied by a hydraulic testing machine. The confining pressure was supplied independently by another oil compressor. The value of confining pressure was measured by a Bourdon gage. The axial load was

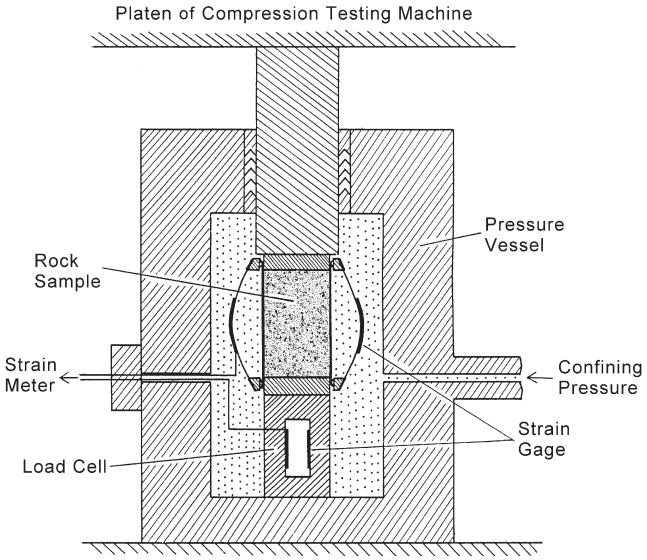

Figure 2.1. Schematic view of the triaxial apparatus.

measured by a load cell situated between a steel end piece fixed to the test specimen and the bottom of the pressure vessel. The load cell, a closed hollow steel cylinder with an electric resistance strain gage bonded to the inside of the cylinder, measured the axial load without any frictional error.

In Fig. 2.2, various methods of the axial strain measurement are shown. The external method (1) in this figure, using a dial gage or differential transformer in which the strain is obtained from the displacement of the piston of the press, is not accurate enough for a precise analysis of the stress-strain curve and it is not applicable for cyclic loading because this system shows a remarkable hysteresis. For precise measurements of strain, the internal method (2) of which the two methods (a) and (b) are schematically shown in Fig. 2.2. In the first method (a), the electric resistance strain gage is bonded directly onto the surface of the rock specimen. This method is highly sensitive and easy-to-use, therefore it is used most often. However, method (a) is unsuitable to measure the mean strain in heterogeneous deformation including microcracks, small faults, etc. and to measure large deformation. In method (b), bending steel plates are fixed to the upper and lower steel end pieces connected to the rock specimen, and shortening of the rock cylinder causes the bending of the thin steel plates. The bending deformation of the plate is measured by the bonded strain gages. As the elastic distortion of steel end pieces is generally negligible because of its slight thickness, the strain gage output indicates the axial strain of the rock specimen. Since this system of strain measurement does not show any appreciable hysteresis for loading and unloading, this method is applicable for cyclic loading experiments, and also is suitable for large deformation measurements.

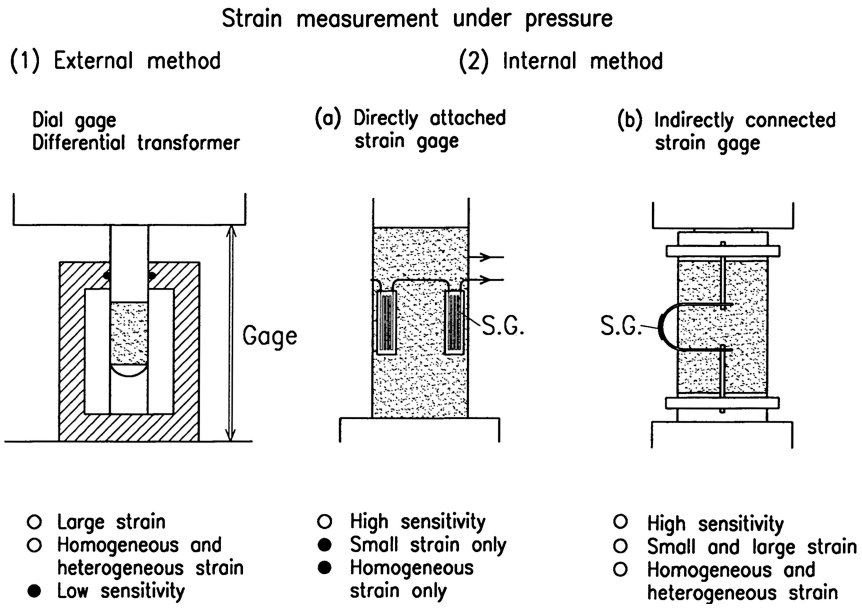

Figure 2.2. Various methods of the axial strain measurement.

However, the behavior of electric resistance type strain gage should be examined under confining pressure, because there was a question that the strain gage might show an appreciable "pressure effect" due to hydrostatic pressure. To examine this "pressure effect", the change in strain measured by the electric resistance strain gage under confining pressure was compared with that in the atmospheric pressure, as shown in Fig. 2.3. Strains (A) and (B) are the axial strains of, respectively, the outside and the inside of the hollow steel cylinder with closed ends under axial compression. Open circles in Fig. 2.3 are in atmospheric pressure (0.1 MPa) and closed circles are in 130 MPa confining pressure. Since the relation between strain (A) and strain (B) is almost similar in both cases, the hydrostatic pressure does not give any significant effect to the gage factor.

Thus, method (b) shown in Fig. 2.2 or Fig. 2.1 is applicable to precise measurements of small and large strains of various rocks under cyclic loadings. The axial load was applied at a nearly constant strain rate of 0.15–0.2 percent per min. The differential stress was reduced to zero at various stages of deformation, the elastic and permanent strains were observed at each stage.

2.1.b *Stress-strain relation*

The rocks tested were a peridotite, a diorite, a granite (strength only), two andesites, a trachyte, three tuffs and a marble. The density and porosity of these rocks are shown in Table 2.1.

The test specimens were compressed to fracture for hard rocks and to 3–4 percent strain for soft rocks, and at various stages of deformation the stress was reduced to

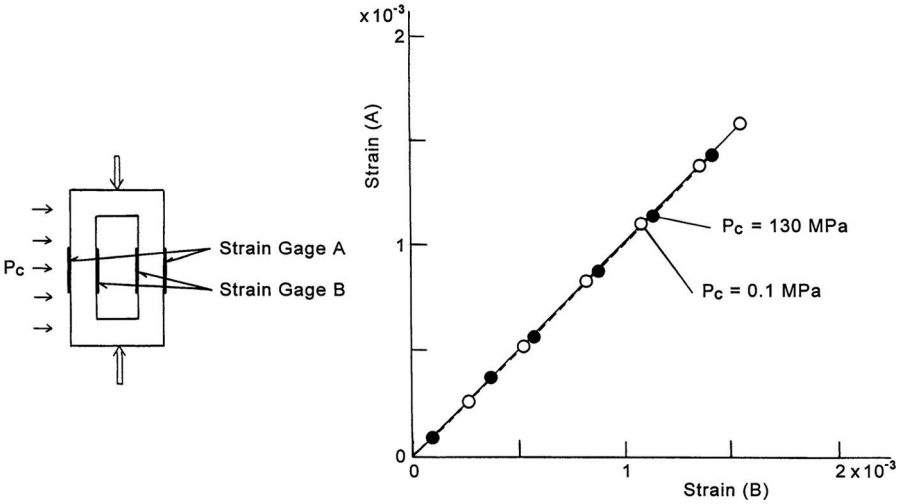

Figure 2.3. Strains (A) and (B) are the axial strains at, respectively, the outer and inner surface of the steel hollow cylinder with closed ends subjected to confining pressure.

Table 2.1. Tested rocks.

No.	Rock	Bulk density (g/cm^3)	Porosity (%)
1.	Nabe-ishi peridotite	3.16	0.02
2.	Orikabe diorite	2.78	0.4
3.	Mannari granite	2.62	0.7
4.	Mito marble	2.69	0.2
5.	Shirochoba andesite	2.45	5.1
6.	Tatsuyama tuff	2.26	10.2
7.	Mizuho trachyte	2.24	8.5
8.	Shinkomatsu andesite	2.17	12.6
9.	Ao-ishi tuff	2.01	17.3
10.	Saku-ishi welded tuff	1.95	21.6

zero or to very small values, then increased again. Stress-strain curves of some of these rocks under the conventional triaxial compression for different values of the confining pressure ($\sigma_2 = \sigma_3$) are shown in Figs. 2.4(a)–2.4(f). The vertical axis is the differential stress ($\sigma_1 - \sigma_3$) in MPa and the horizontal axis is the strain in percent.

The experimental results show that compact igneous rocks are very brittle and become markedly stronger with the increase of confining pressure, while other porous soft rocks become ductile even under low confining pressure. However, the precise feature of these curves suggests complex processes of deformation. For example, the initial part of deformation before yielding, the so-called *elastic part*, is significantly curved and includes appreciable permanent deformation in many cases. The simple

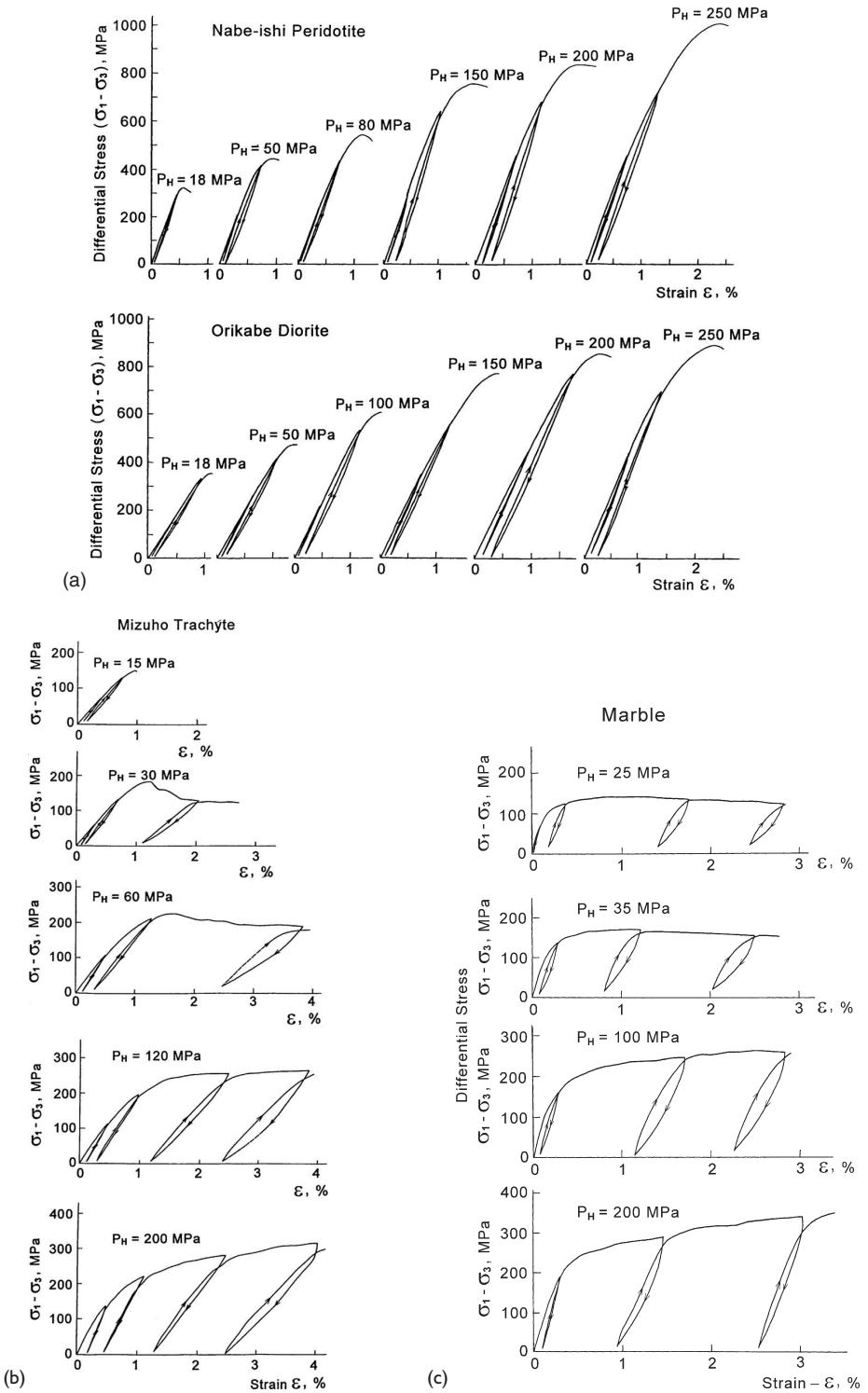

Figure 2.4(a)–(f). Stress-strain curves under cyclic axial loading of various kinds of rocks. P_H: confining pressure.

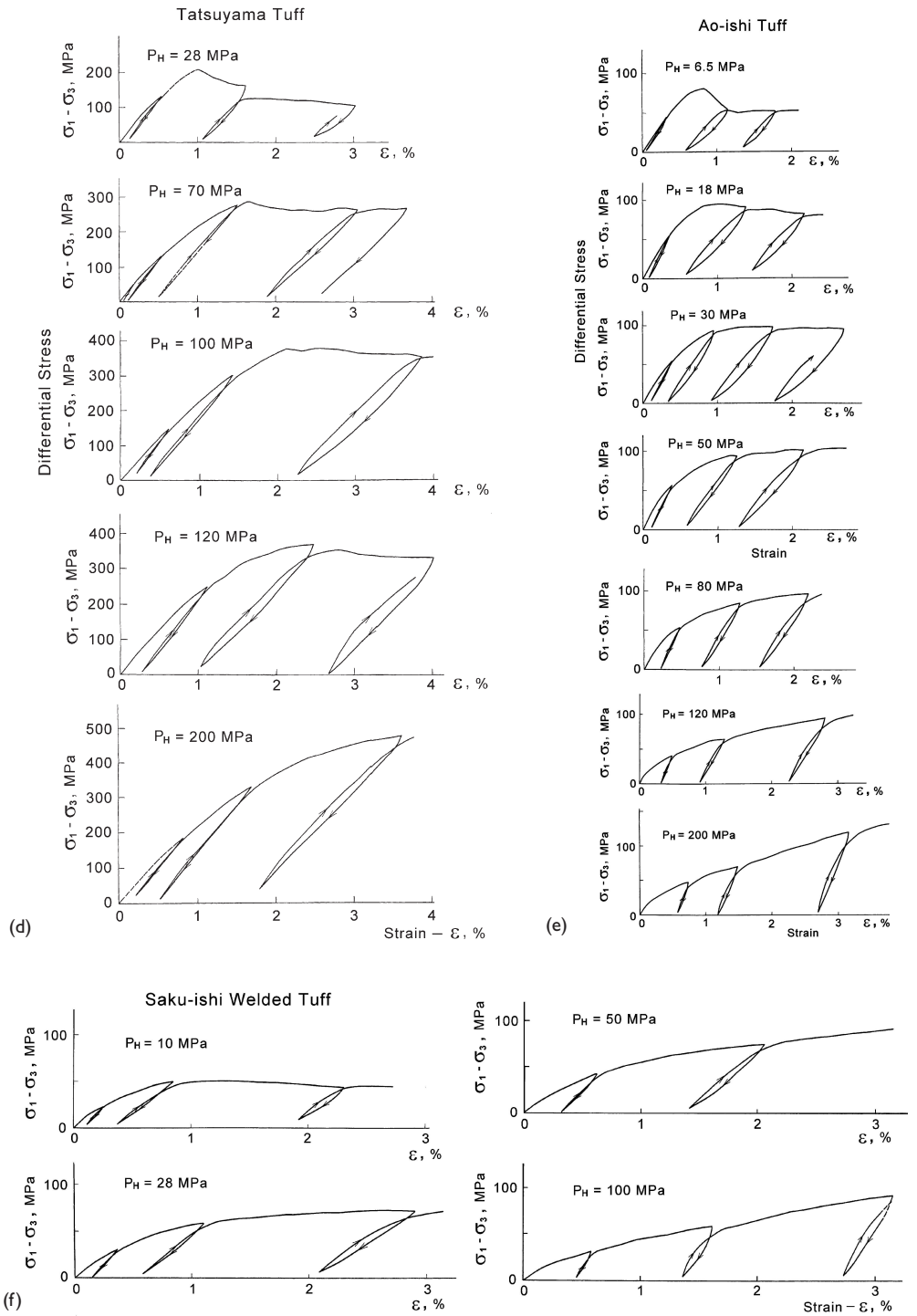

Figure 2.4. (*Continued*)

slope of the stress-strain curve is different from the elastic modulus which is defined in the later discussion.

The terms *brittle* and *ductile* which are used in this book are understood as follows. Brittle behavior is characterized by a sudden change of slope in the stress-strain curve near the yield point followed by a complete loss of cohesion or an appreciable drop in differential stress. Ductile behavior is characterized by the deformation without any downward slope after the yield point. Further discussions of the definition of *brittle*, *ductile*, and *yielding* will be presented later.

2.1.c *Modulus of elasticity*

When the rock specimen is compressed to a point P in Fig. 2.5 and then unloaded to zero differential stress and then reloaded, the branches (P2Q, Q3P) are different from the virgin loading curve (O1P) in many cases, as shown schematically in Fig. 2.5. The unloading and reloading curves usually differ little from each other and form a narrow loop (P2Q3). The reloading curve (Q34) passes very near the point P from which the unloading branch drops down and continues to the virgin loading curve (O1P). This narrow loop circumscribed by the unloading and reloading branches may be approximately substituted by a straight line $\overline{PQ}$. The slope of this line is taken as the mean Young's modulus.

Figure 2.6 show the relation between Young's modulus (E) and the total strain (ε), which is defined in Fig. 2.5, for different values of confining pressure. According to this result, Young's modulus differs considerably at various stages of deformation. In compact igneous rocks, Young's modulus is nearly constant until their fracture. In other porous rocks, it generally decreases with increasing strain (ε), as seen in Fig. 2.6. However, the modulus (E) of some ductile rocks (tuffs and marble) under high confining pressure begins to increase with strain just after the yielding. The marked decrease of Young's modulus (E) with increasing strain (ε) is attributed to the microfracturing in these rock specimens, and the increase of Young's modulus (E) in a large

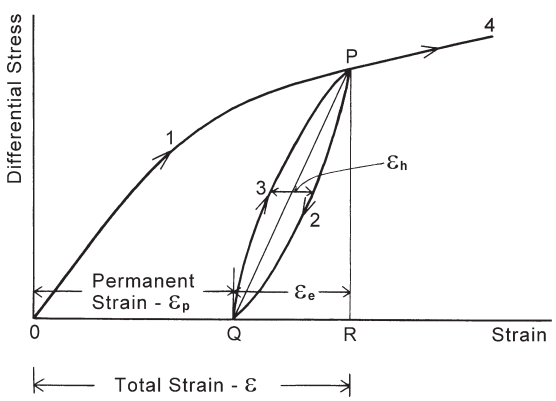

Figure 2.5. Typical stress-strain curves under cyclic loading.

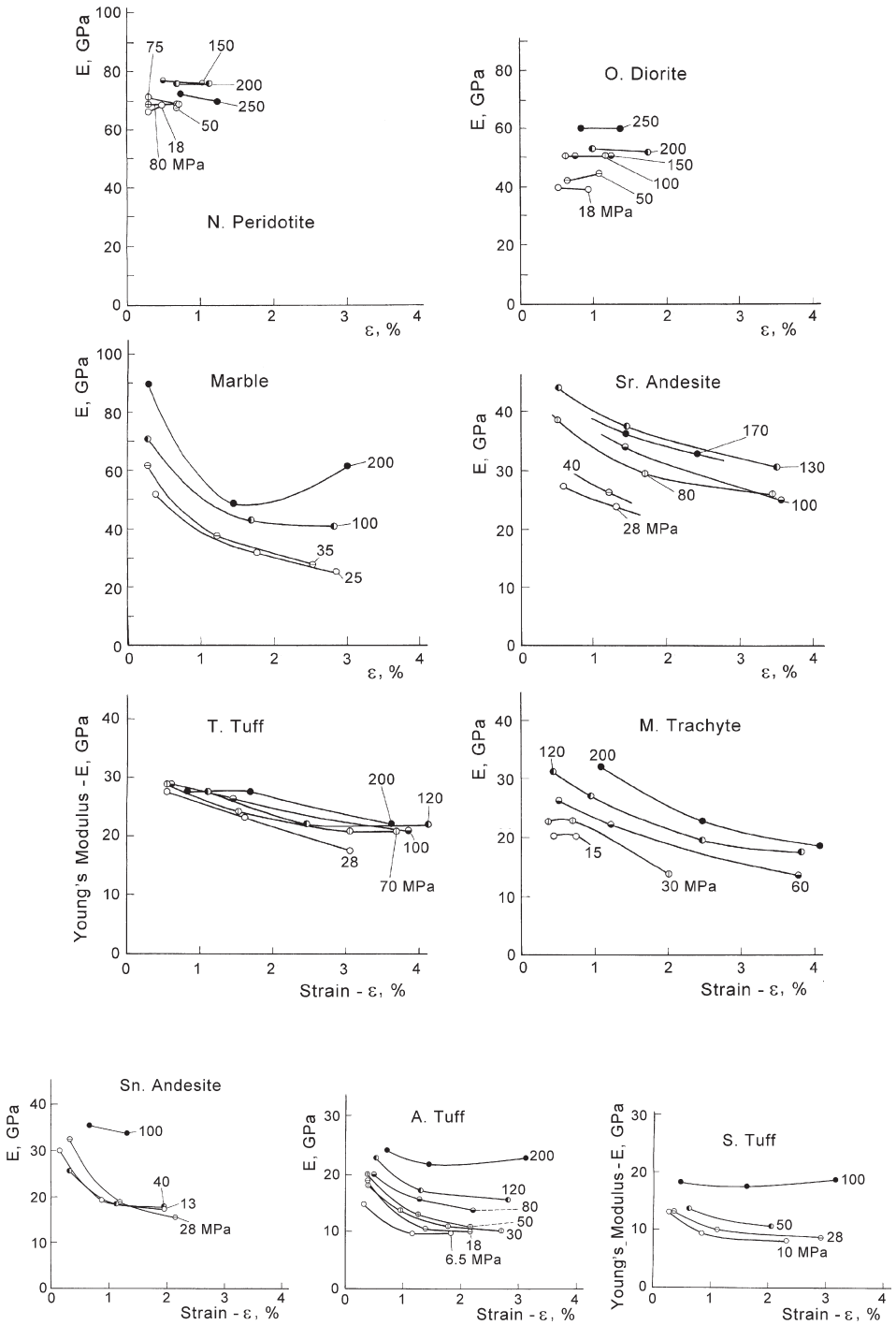

Figure 2.6. Relation between Young's modulus (E) and the total strain (ε).

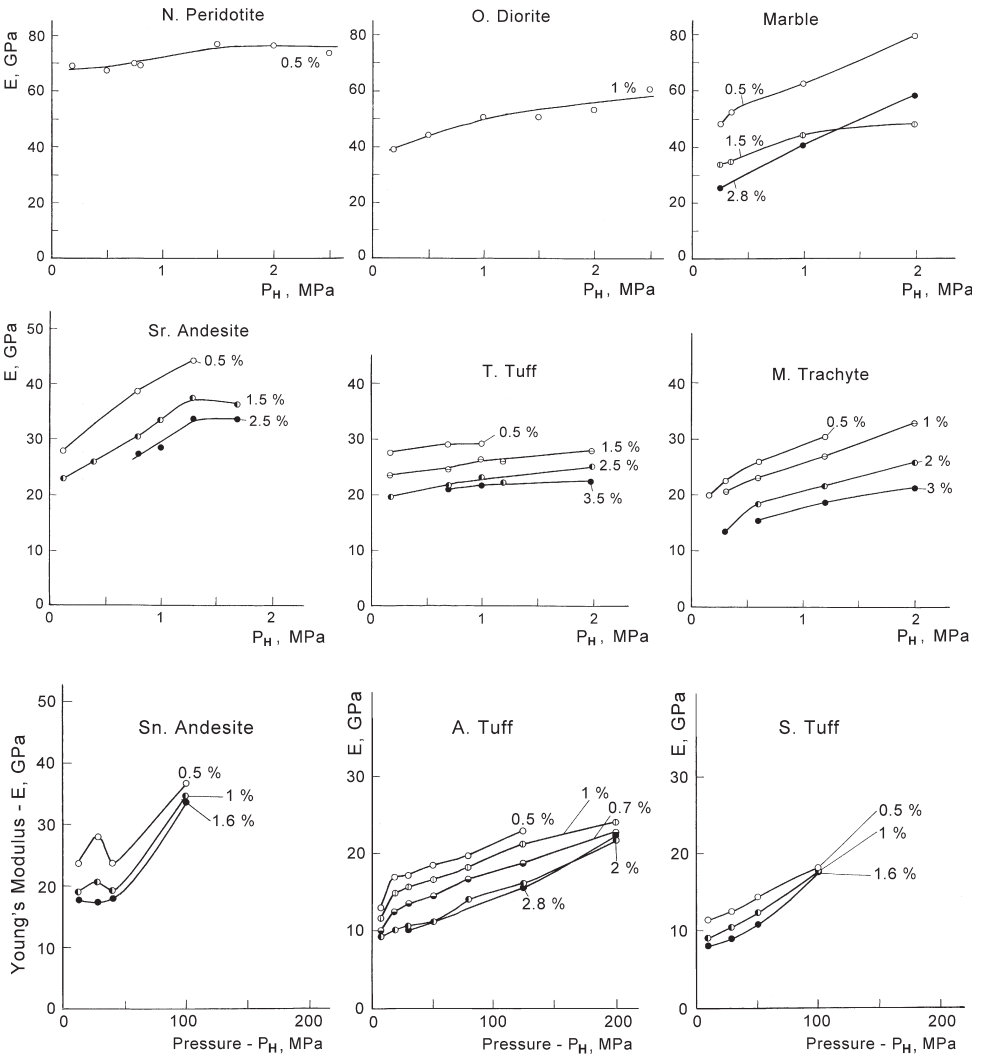

Figure 2.7. Relation between Young's modulus and the confining pressure. Values of the total axial strain are given for each curve.

deformation stage under high confining pressure in soft rocks can be attributed to compaction of fractured rock specimens.

The relations between Young's modulus (E) and confining pressure ($\sigma_3 = \sigma_2$) are shown for different values of strain in Fig. 2.7. Normally, Young's modulus increases with pressure. The modulus of Nabe-ishi peridotite, which is the most compact rock (porosity 0.02%) among the tested rocks, is largest and increases slightly with confining pressure. The modulus E of Orikabe diorite (porosity 0.4%) is lower than that of peridotite and its increase with confining pressure is more appreciable. The results obtained for igneous compact rocks are consistent with similar preceding

experiments (e.g., Brace, 1964), and with results of elastic wave velocity measurement (Birch, 1960). In more porous rocks, Young's modulus increases more markedly with confining pressure, as shown in Fig. 2.7.

The pressure dependence of Young's modulus in Shinkomatsu andesite is abnormal at lower pressures, as seen in Fig. 2.7. Young's modulus increases with a pressure increase to 28 MPa and drops noticeably at 40 MPa. This drop in Young's modulus is not so clear at larger strains. This abnormal change in Young's modulus seems to be attributed to the mechanical structure of this rock. That is, the porosity of this volcanic rock is markedly high (12.6%) and most pores are isolated round voids in a continuous framework, while other porous sedimentary rocks have wedge-like openings between grains. The above-mentioned abnormal behavior of the andesite seems to be due to the fracturing of this rock's framework by the confining pressure.

2.1.d *Permanent strain*

The strain of stressed rocks is partly elastic and partly permanent. The elastic strain is obtained as a recovered deformation by unloading to zero differential stress while the permanent strain is obtained as an unrecovered deformation (Fig. 2.5). This permanent strain includes various types of unrecoverable deformation due to dislocation, viscous flow, micro-fracturing, etc. and so it increases to some degree with the decrease of strain rate (e.g., Heard, 1963).

In Fig. 2.8, the relation between the permanent strain (ε_p) and the total strain (ε) is shown for different confining pressures. It should be noted that the permanent strain is found even at an initial stage of deformation in most rocks. In compact igneous rocks which are very brittle, the permanent strain appears slightly in the nearly linear part of stress-strain curve and increases abruptly from a proportional limit. In some porous silicate rocks, such as Tatsuyama tuff (porosity 10.2%), the appreciable permanent deformation increases linearly at the initial stage and the slope of this curve increases suddenly at some stage. In highly porous silicate rocks, such as Ao-ishi tuff (porosity 17.3%), the permanent strain is very large and increases continuously without any such sudden change in the slope of curve, particularly under higher confining pressure. In carbonate rocks, which show remarkable ductile behavior, the $\varepsilon_p - \varepsilon$ relation is very different from those of silicate rocks. The case of Mito marble (porosity 0.2%) is shown in Fig. 2.8. The ratio $\varepsilon_p/\varepsilon$ is very large (60–80%) except for the initial stage of deformation, and nearly independent of confining pressure. The main part of large deformation of marble is permanent, as can be seen in Figs. 2.4(c) and 2.8.

2.1.e *Effects of previous loading*

As mentioned above, rocks are not completely elastic materials and they show remarkable plasticity; during the deformation of rocks microfracturing occur in many cases. Therefore, the stress-strain relation is affected by a history of deformation. If the effect of the previous deformation is clarified, a history of deformation of rocks may be deduced from the present mechanical property. As a preliminary step from this

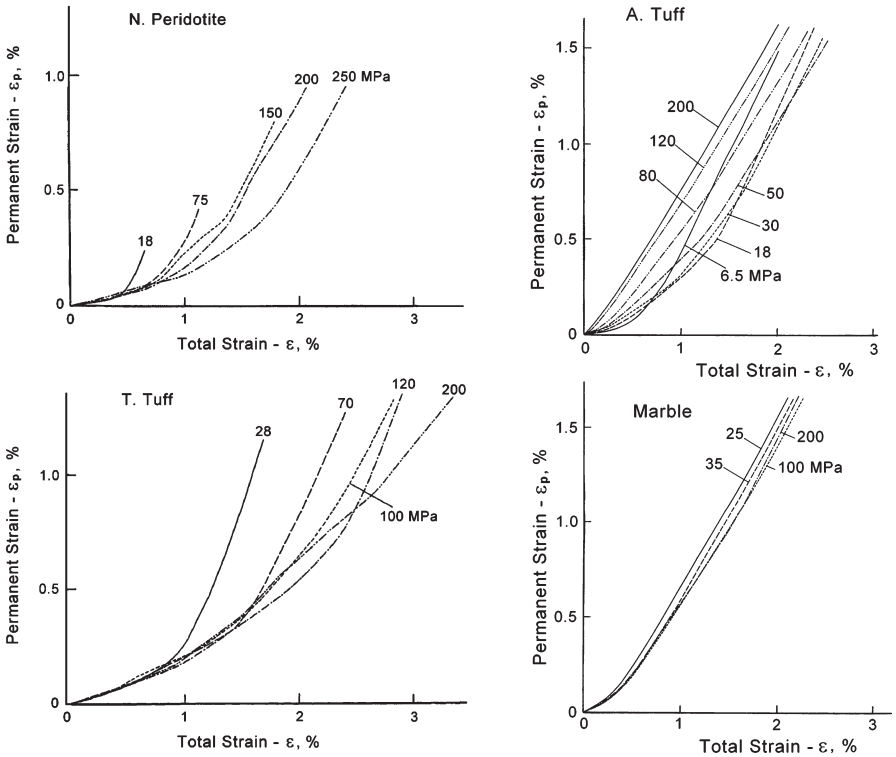

Figure 2.8. Relation between the permanent strain and the total strain. Values of the confining pressure are given for each curve.

viewpoint, an effect of previous loading of Ao-ishi tuff was measured in some simple cases (Mogi, 1965).

2.1.e.1 *Hydrostatic pressure*

An effect of previously applied hydrostatic pressure was studied. Ao-ishi tuff specimens were initially exposed to hydrostatic pressure of 80 MPa and 200 MPa. Thereafter, these specimens and a virgin specimen were tested under conventional triaxial compression conditions at 18 MPa confining pressure. Curves (B) and (C) in Fig. 2.9 show the stress-strain characteristics of specimens which were initially exposed to 80 MPa and 200 MPa hydrostatic pressure respectively, and curve (A) is that of the virgin specimen. Both the compressive strength and Young's modulus in the case of 80 MPa hydrostatic pressure are not significantly different from those of the virgin rock. On the other hand, the compressive strength and Young's modulus in the case of 200 MPa are markedly lower than those of the virgin rock. From this result, it may be deduced that this rock has not been buried at a larger depth than several kilometers.

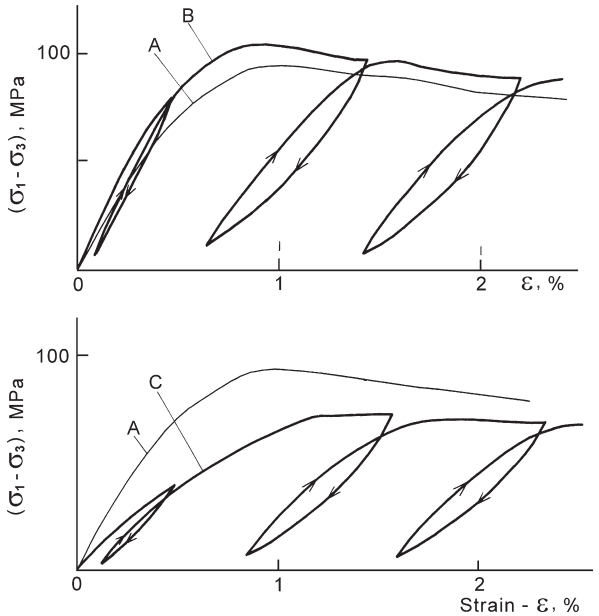

Figure 2.9. Stress-strain curves of Ao-ishi tuff under 18 MPa confining pressure. (A): virgin specimen; (B): specimen previously exposed to 80 MPa hydrostatic pressure; (C): specimen previously exposed to 200 MPa hydrostatic pressure.

2.1.e.2 *Axial compression*

As can be seen from the stress-strain curves obtained by cyclic loading, Young's modulus and plasticity are affected by a previous compression. After initial compression, the stress-strain curve markedly changes in comparison to that of virgin rocks. The experimental result of Ao-ishi tuff is shown in Fig. 2.10. A specimen was axially shortened by 2.2 percent by the conventional triaxial compression test (confining pressure 80 MPa). After being left 18 hours at atmospheric pressure, the specimen was tested again by compression under 80 MPa confining pressure [curve (2)]. Young's modulus decreases somewhat due to previous loading, but its value corresponds to that in deformation continued without such a break in loading. The stress-strain curve before yielding in curve (2) is nearly linear and the permanent strain at this stage is smaller as compared with the initial part of the deformation of the virgin rock. The most noticeable change between the two curves (1) and (2) is the marked increase of the apparent yield stress in the previously loaded specimen. From this result, it may be deduced that the yield stress corresponds to the magnitude of previously applied stress in such cases.

Effects of previous loading may be complex. However, a history of deformation of rock specimen is more or less preserved in mechanical properties, such as elasticity, plasticity, fracture strength, deformation characteristics in repeated loadings, and other qualities. Thus, the deformation experiments from this point of view may be useful for studying the mechanical history of the earth's materials. After many years of

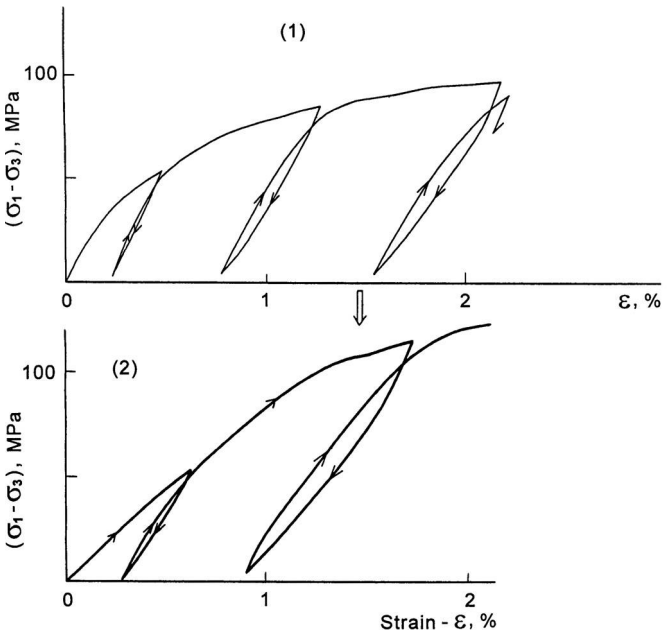

Figure 2.10. Stress-strain curves of Ao-ishi tuff under 80 MPa confining pressure. (1): virgin specimen; (2): specimen previously shortened by 2.2%.

this preliminary experiment, more careful experiments have been conducted from the similar standpoint. For example, Yamamoto et al. (1990) developed a method for estimating crustal stress by measurements of the mechanical history of rock specimens.

2.1.f *Yield stress*

Strength in the brittle state is the maximum stress achieved during an experiment. This value is definitely determined. However, failure strength in the ductile state, namely yield stress, is usually not so definite. Generally, the yield stress is the stress at which the sudden transition from elastic to plastic deformation state takes place, and so the stress at the knee of the stress-strain curves is taken as the yield stress (e.g., Robertson, 1955). In some rocks, the knee of the stress-strain curve is clear and the determination of yield stress is easily possible. However, other rocks show a gradual transition from elastic to plastic stage, that is, the slope of the stress-strain curve varies gradually. In this case, the definite determination of yield stress is difficult.

Sometimes the yield point is defined as a point having an appreciable limit value of permanent deformation. This definition is also not always suitable for various rocks, because the value of the permanent strain at the marked break of the stress-strain curve is not constant and varies widely.

If the yielding is understood in a wide sense, the yield stress of rocks may be more generally defined in the following way. The local yielding begins to occur even under

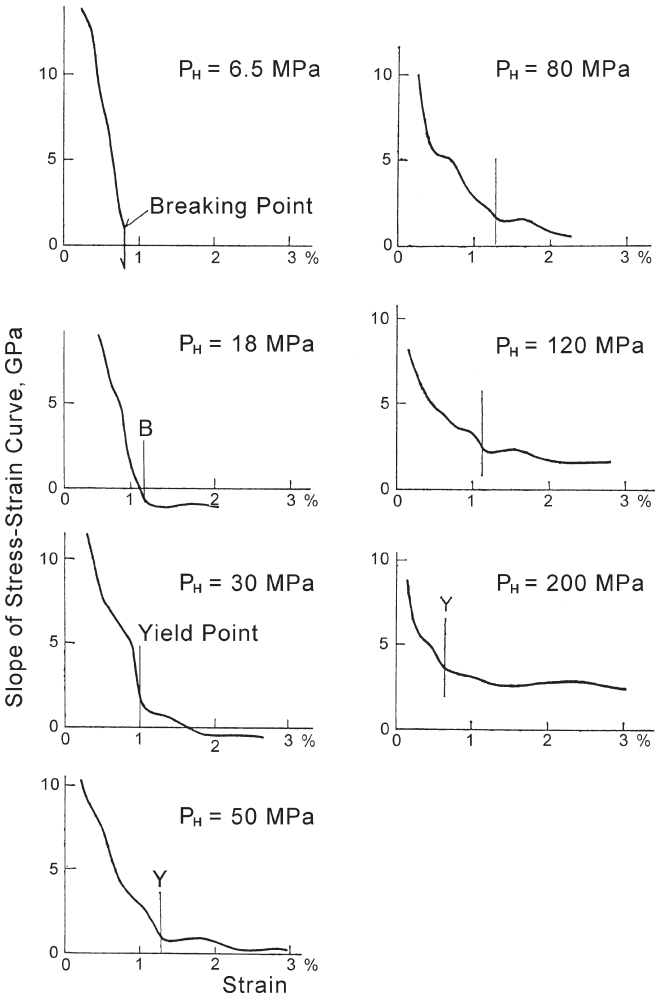

Figure 2.11. Relation between $\Delta(\sigma_1 - \sigma_3)/\Delta\varepsilon$ and strain (ε) for Ao-ishi tuff. Values of confining pressure are given for each curve.

low stress, because the stress in the rock specimen having nonuniform structures distributes concentratively around structural irregular points. The yielding in such nonuniform materials takes place gradually in a wide range of stress values, and the macroscopic yielding may be completed at a certain stress value. This terminal stress is treated as yield stress. In fact, the slope of the stress-strain curve decreases gradually with the increase of strain and becomes nearly constant at the yield stress in many cases. This definition is also consistent with the usual definition in the case characterized by a marked break of the stress-strain curve. Fig. 2.11 shows the relation between the slope of the stress-strain curve $[\Delta(\sigma_1 - \sigma_3)/\Delta\varepsilon]$ and the axial strain (ε) of Ao-ishi tuff. It is suitable that, the point at which $\Delta\sigma/\Delta\varepsilon$ becomes nearly constant is taken as the yield point.

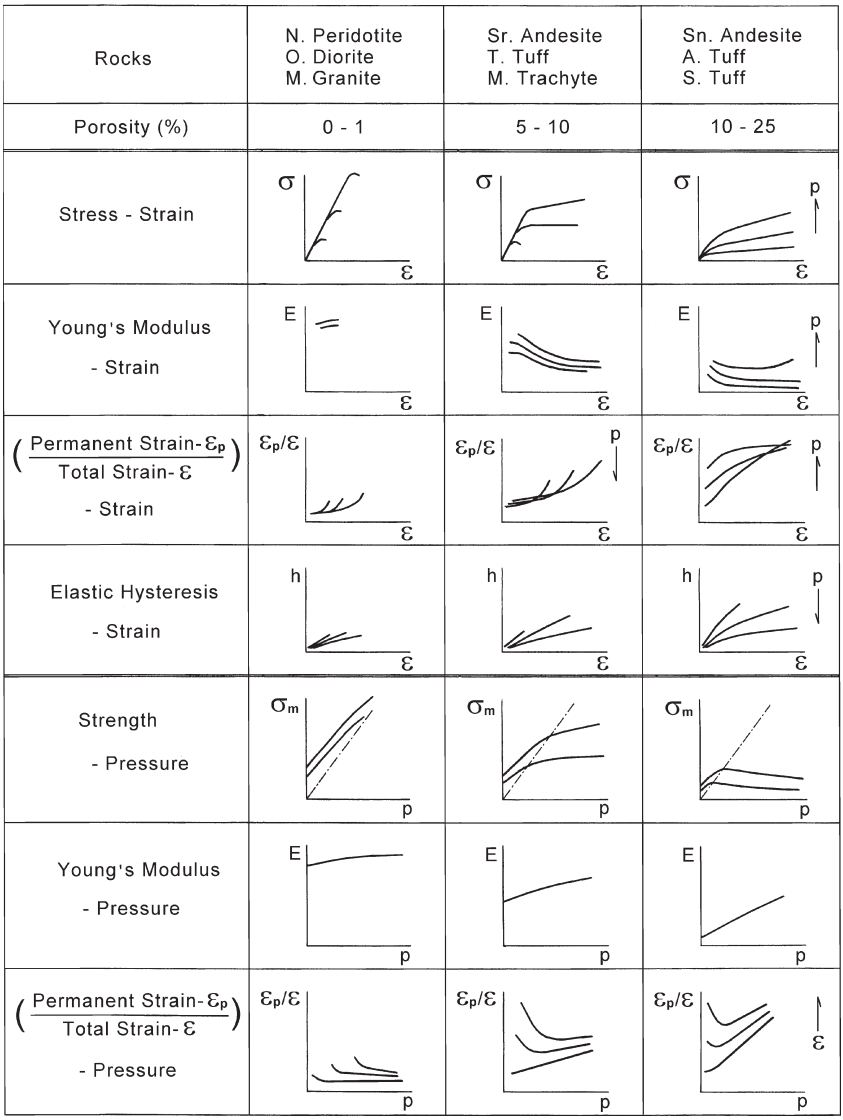

Figure 2.12. Summary of the deformation characteristics of silicate rocks under confining pressure and at room temperature (Mogi, 1965).

2.1.g *Summary of the deformation characteristics*

Using the conventional triaxial test and the indirect strain gage method, the stress-strain curves in cyclic loading were obtained for different types of rocks. The tested silicate rocks can be divided into three groups according to their mechanical properties. The mechanical properties of these rocks are roughly summarized in Fig. 2.12. The range of porosity in these rocks is tabulated in this figure. From this result, it can

be clearly seen that porosity is the most important factor for mechanical properties in silicate rocks. The mechanical properties of the marble are significantly different from those of silicate rocks. Although the porosity of the marble is very small (about 0.2%), its properties are nearly similar to the third group in appearance. This shows that the mineral composition is also an important factor in mechanical behavior in rock deformation under pressure.

2.2 PRESSURE DEPENDENCE OF COMPRESSIVE STRENGTH AND BRITTLE-DUCTILE TRANSITION

2.2.a *Relation between strength and confining pressure*

As mentioned in the preceding section, the compressive strength of rocks generally increases with increasing confining pressure. The pressure dependence of

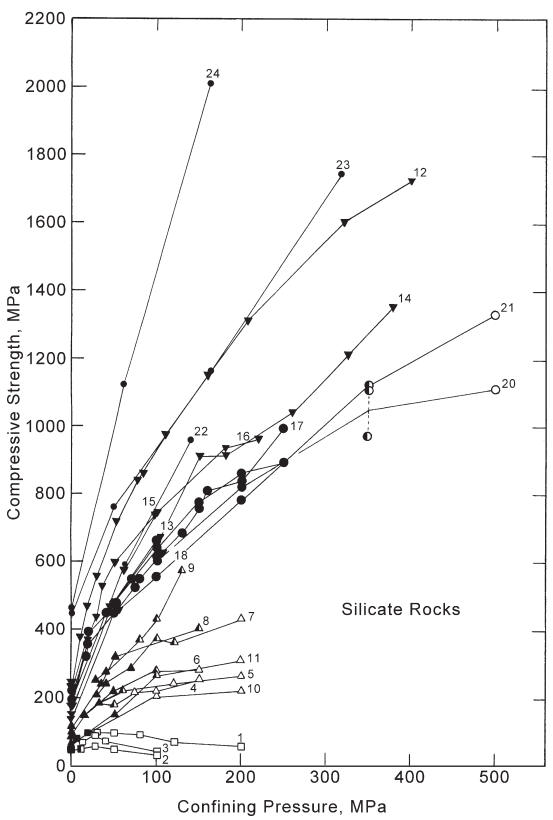

Figure 2.13. Relation between compressive strength and confining pressure for silicate rocks. Numbers given for each curve correspond to rocks listed in Table 2.2. Closed symbols: brittle behavior; semi-closed: transitional behavior; open: ductile behavior.

rock strength has been experimentally studied by many investigators (e.g., Adams and Nicolson, 1901; von Kármán, 1936; Robertson, 1955; Griggs, 1936; Handin and Hager, 1957; Brace, 1964; Mogi, 1966a,b). Fracture strength of brittle hard rocks increases markedly with increasing pressure. On the other hand, the yield stress of ductile rocks, such as some limestones and marbles, does not increase appreciably.

Compressive strengths ($\sigma_1 - \sigma_3$) of silicate rocks and carbonate rocks are shown as functions of confining pressure ($\sigma_2 = \sigma_3$) in Fig. 2.13 and Fig. 2.14, respectively (Mogi, 1966a). Data in these figures are taken from references listed in Table 2.2. In the figures, the closed, semi-closed and open symbols indicate brittle, transitional and ductile behavior, respectively. These rocks are divided into several groups for convenience, as shown in Table 2.2. These strength-pressure curves are more or less concave downward with a roughly similar shape. Fig. 2.15 shows the relation between ($\mathbf{C}$–$\mathbf{C}_0$) and confining pressure of silicate rocks in logarithmic scales, where $\mathbf{C}$ and $\mathbf{C}_0$ are compressive strength at elevated confining pressures and at atmospheric pressure, respectively. As shown for Kitashirakawa granite by Matsushima (1960), these strength data are expressed nearly by the power law of confining pressure. Such compilation of strength data and their plot have been given by a number of investigators (e.g., Handin, 1966).

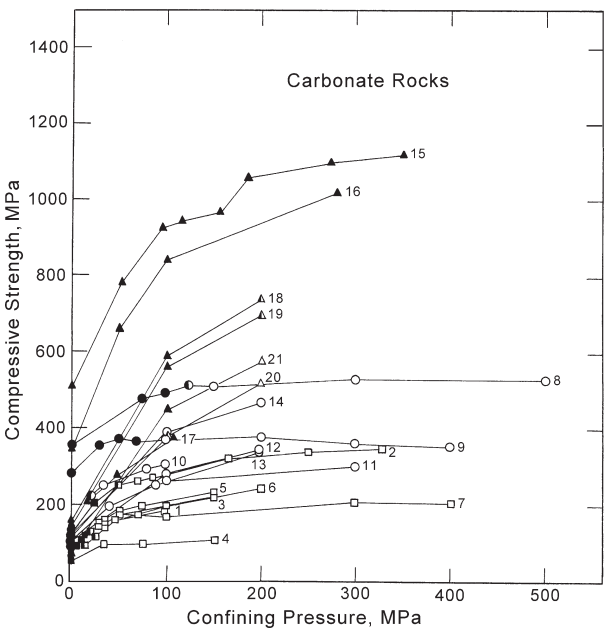

Figure 2.14. Relation between compressive strength and confining pressure for carbonate rocks. Numbers given for each curve correspond to rocks listed in Table 2.2. Closed symbols: brittle behavior; semi-closed: transitional behavior; open: ductile behavior.

Table 2.2. A list of rocks.

No.	Rock	Tested by	Grouping
A. Silicate rocks			
1.	Aoishi Tuff	Mogi (1965)	S_1 (Highly porous; Porosity >10%)
2.	Sakuishi Welded Tuff	Mogi (1965)	
3.	Shinkomatsu Andesite	Mogi (1965)	
4.	Mizuho Trachyte (1)	Mogi (1964)	S_2 (Porous; Porosity: 1–10%)
5.	Mizuho Trachyte (2)	Mogi (1965)	
6.	Tatsuyama Tuff (1)	Mogi (1964)	
7.	Tatsuyama Tuff (2)	Mogi (1965)	
8.	Shirochoba Andesite (1)	Mogi (1964)	
9.	Shirochoba Andesite (2)	Mogi (1965)	
10.	Bartlesville Sandstone	Handin & Hager (1957)	
11.	Barns Sandstone (1)	Handin & Hager (1957)	
12.	Westerly Granite	Mogi (1966)	S_3^* (Nonporous; Porosity <1%)
13.	Barre Granite	Robertson (1955)	
14.	Kitashirakawa Granite	Matsushima (1960)	
15.	Inada Granite	Mogi (1964)	
16.	Mannari Granite	Mogi (1965)	
17.	Nabeishi Peridotite	Mogi (1965)	
18.	Ukigane Diorite	Mogi (1964)	
19.	Orikabe Diorite	Mogi (1965)	
20.	Cabramurra Serpentinite	Raleigh & Paterson (1965)	
21.	Tumut Pond Serpentinite	Raleigh & Paterson (1965)	
22.	Pala Gabbro	Serdengecti et al. (1961)	
23.	Frederic Diabase	Brace (1964)	
24.	Cheshire Quartzite	Brace (1964)	
B. Carbonate rocks			
1.	Wombeyan Marble	Paterson (1958)	*CM* (Marble)
2.	Carrara Marble	Kármán (1911)	
3.	Yamaguchi Marble (Fine)	Mogi (1964)	
4.	Yamaguchi Marble (Coarse)	Mogi (1964)	
5.	Mito Marble (1)	Mogi (1964)	
6.	Mito Marble (2)	Mogi (1965)	
7.	Danby Marble	Robertson (1955)	
8.	Solnhofen Limestone (1)	Heard (1960)	*CL* (Limestone)
9.	Solnhofen Limestone (2)	Robertson (1955)	
10.	Wells Station Limestone	Paterson (1958)	
11.	Becraft Limestone	Robertson (1955)	
12.	Devonian Limestone	Handin & Hager (1957)	
13.	Fusselman Limestone	Handin & Hager (1957)	
14.	Wolfcamp Limestone	Handin & Hager (1957)	
15.	Blair Dolomite (1)	Brace (1964)	*CD* (Dolomite)
16.	Blair Dolomite (2)	Robertson (1955)	
17.	Webatuck Dolomite	Brace (1964)	
18.	Clear Fork Dolomite	Handin & Hager (1957)	
19.	Fusselman Dolomite	Handin & Hager (1957)	
20.	Hasmark Dolomite (T)	Handin & Hager (1957)	
21.	Luning Dolomite	Handin & Hager (1957)	

Silicate rocks of No. 12–16 and No. 17–21 are denoted as S_3G and S_3P, respectively.

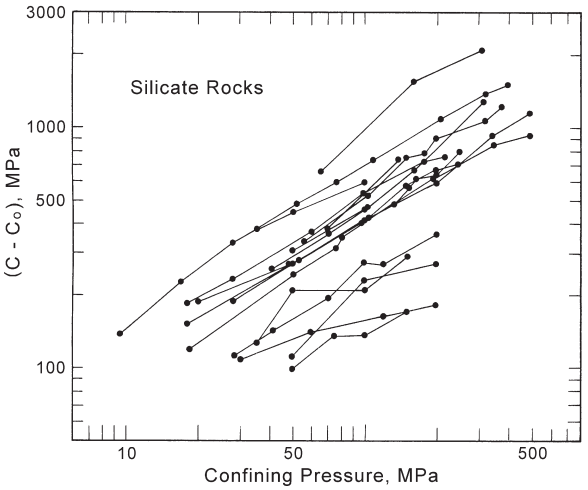

Figure 2.15. Relation between ($C–C_0$) and confining pressure for silicate rocks, except for very porous rocks (S_1)). C: compressive strength, C_0: strength at atmospheric pressure.

However, most of these experiments have been carried out using the conventional test, which uses a short cylinder and is accompanied by stress concentration and the clamping effect at the end part of the specimen, as mentioned in Chapter 1. Therefore, compressive strength at atmospheric pressure and under low confining pressure should be measured by use of the revised specimen design. The experimental results for Westerly granite and Dunham dolomite which were obtained by the revised method are summarized in Table 2.3 and Figs. 2.16–2.17 (Mogi, 1966b). The larger circles in these figures represent the average strength of samples whose length/diameter ratio was greater than its critical value (2.5), so their reliability is high. The smaller circles were obtained from one or two experiments using specimens of length/diameter ratio 2.5, so their reliability is limited.

Fracture of Westerly granite was always very violent and explosive, and followed by a sudden stress drop under tested confining pressure (<400 MPa). It is noteworthy that the strength-pressure curve is not linear, but is concave downwards, especially at low pressure. This result seems to be inconsistent with some fracture criteria which predict a linear relation. In dolomite, strength increases nearly linearly with pressure.

Fracture angles in both rocks are shown in Fig. 2.16(b) and 2.17(b). Since the fracture angles are predicted from the Mohr envelope curve based on strength data, the observed fracture angles are also compared with the predicted angles by the Mohr envelope curves in these figures. In Dunham dolomite, the difference is small (0°–2.5°) and not systematic, so the Mohr theory would seem to apply here. In Westerly granite, the calculated curve is parallel to the observed curve and the calculated values are slightly lower than the observed values. The difference between them is (2°–4°) under lower confining pressure and decreases with pressure. The Mohr theory assumes that fracture occurs by shearing in a slip plane which depends on the value

Table 2.3. Strength and fracture angle under different pressures.

Rock	Confining pressure (MPa)	Differential stress (MPa)	Observed fracture angle	Calculated fracture angle
Dunham dolomite	0.1*	209	20°	19° (?)
	8.2	289	20°	20.5°
	10.8	296	21°	21°
	18.0*	344	20°	22°
	21.6	367	22°	24.5°
	33.0*	412	25°	26° (?)
Westerly granite	0.1*	239	19°	–
	9.5	378	19.5°	15°
	17.0*	467	20.5°	17.5°
	27.5	555	22.5°	20°
	51.0*	720	24°	22°
	77.0	840	–	23°
	108.0*	977	26°	24.5°
	207.0	1308	–	27°
	321.0**	1597	32°	30.5°
	400.0**	1717	35°	34.5° (?)

* Average value from several tests.
** Average value from two tests.

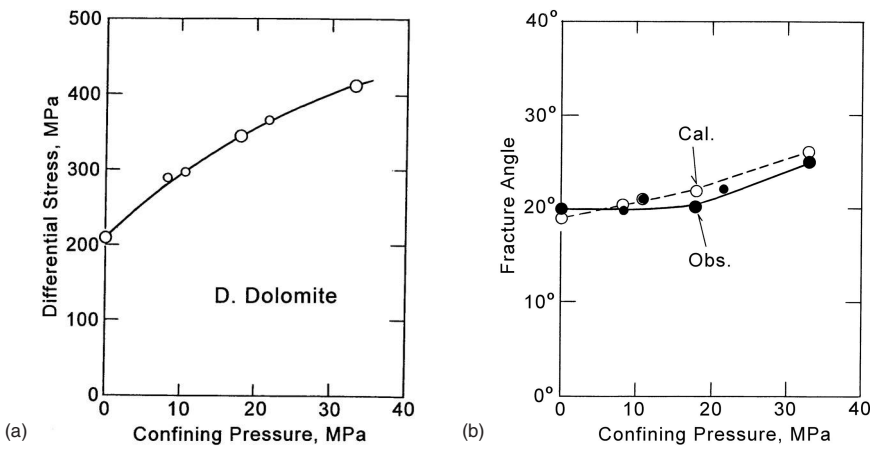

Figure 2.16. (a) Relation between compressive strength and confining pressure for Dunham dolomite. (b) Relation between fracture angle and confining pressure for Dunham dolomite. Closed circle: observed angle; open circle: angle calculated from the Mohr envelope (Mogi, 1966b).

of the normal stress on the plane. The fracture in dolomite is a typical shear type. The fracture in granite specimens is also clearly of a shear type under high confining pressure, but under atmospheric or low pressure is often curved and quite irregular. The difference noted above between observation and calculation may be a manifestation

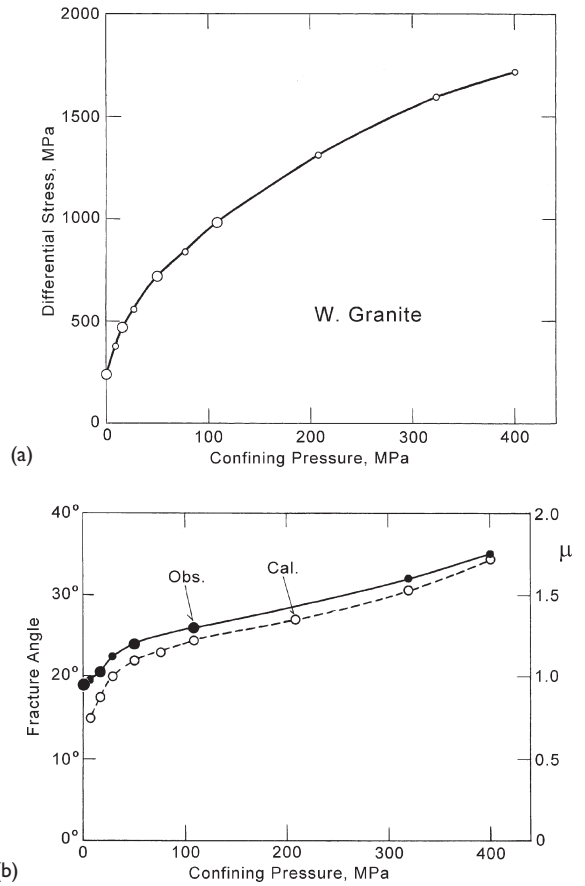

Figure 2.17. (a) Relation between compressive strength and confining pressure for Westerly granite (Mogi, 1966b). (b) Relation between fracture angle and confining pressure for Westerly granite. Closed circle: observed angle; open circle: angle calculated from the Mohr envelope.

of these irregularities. However, the difference (average 2.2°) between them may not be significant because the accuracy of angle measurement in granite is not very high.

From these precise measurements, it may be concluded that the Mohr theory applies rather well to shear fracture of a granite and dolomite in conventional triaxial compression ($\sigma_2 = \sigma_3$).

2.2.b *The Coulomb-Mohr fracture criterion*

As mentioned above, the compressive strength of brittle rocks is very dependent on confining pressure. Several fracture criteria have been proposed to correlate observed data. Among them, the Coulomb criterion which was introduced by Coulomb (1773), is the simplest and most widely applicable and used for prediction of the effect of confining pressure. The criterion states that shear fracture takes place when the shear stress

(τ) becomes equal to the sum of the cohesive shear strength (τ_0) and the product of the coefficient of internal friction (μ_i) and the normal stress (σ_n) across the fracture plane:

$$\tau = \tau_0 + \mu_i \sigma_n \tag{2.2}$$

If pore-fluid pressure exists, the role of normal pressure is supplanted by the effective normal pressure (Terzaghi, 1945). The Coulomb equation (2.2) is similar to the following equation for frictional sliding on external surfaces (Jaeger, 1959; Byerlee, 1967):

$$\tau = \mathbf{S}_0 + \mu \sigma_n \tag{2.3}$$

where τ is the frictional resistance, σ_n is the normal stress, μ is the coefficient of external friction, and $\mathbf{S}_0$ is a small constant. By comparison of Equations (2.2) and (2.3), it is suggested that μ_i in Equation (2.2) is similar to μ in Equation (2.3). The second term in the right hand side of Equation (2.2) was often interpreted as frictional resistance.

However, Handin (1969) emphasized that the physics of the Coulomb equation might be obscure. He noted that until the cohesion of rock is broken, no sliding surface exists in the intact body, and thus, the Coulomb equation seems to be contradictory, or the concept of internal friction is unsatisfactory. Thereafter, several investigators have also argued that the conventional obvious interpretation of the Coulomb fracture criterion cannot be correct because there is no slip on the fracture plane until after fracture (e.g., Scholz, 1990, p. 14; to some extent Paterson, 1978, p. 25).

On the other hand, the author (Mogi, 1974) proposed a very simple model for physical interpretation of the Coulomb fracture criterion. Recently, Savage, Byerlee and Lockner (1996) extended this model to include the Mohr fracture criterion. In the following, the Coulomb-Mohr fracture criterion is discussed from this point of view.

According to dilatancy and acoustic emission measurements which will be mentioned in later chapters, a number of micro-fractures occur during the deformational process prior to the macroscopic fracture. Fig. 2.18(A) shows schematically the locations of cracks along the eventual fault plane. To simplify the discussion, the area of eventual fault plane (F–F') just before the fracture is divided into the three parts, $\mathbf{A}_1$, $\mathbf{A}_2$, and $\mathbf{A}_3$ [Fig. 2.18(B)]. $\mathbf{A}_1$ is the area which is still intact, $\mathbf{A}_2$ is the total area of closed crack surfaces, and $\mathbf{A}_3$ is the total area of open crack surfaces. Since the open cracks have no effect in the shear resistance, the effect of $\mathbf{A}_3$ can be ignored as the first step. Furthermore, it is assumed that the total shearing resistance ($\mathbf{T}$) at the macroscopic shear fracture is the sum of the shearing resistance ($\mathbf{T}_1$) in the intact part ($\mathbf{A}_1$), which is independent of normal pressure, and the shearing resistance ($\mathbf{T}_2$) in the closed cracks ($\mathbf{A}_2$), which is simply assumed to be the frictional resistance. Therefore the shearing stress (τ) at fracture is:

$$\begin{aligned} \tau &= \mathbf{T}/\mathbf{A} \\ &= \mathbf{T}_1/\mathbf{A} + \mathbf{T}_2/\mathbf{A} \qquad (2.4) \\ &= \tau_1(\mathbf{A}_1/\mathbf{A}) + \mu\sigma_n(\mathbf{A}_2/\mathbf{A}) \qquad (2.5) \end{aligned}$$

where τ_1 is the inherent shearing strength of the intact part which is independent of pressure and μ is the coefficient of external friction. From the comparison of

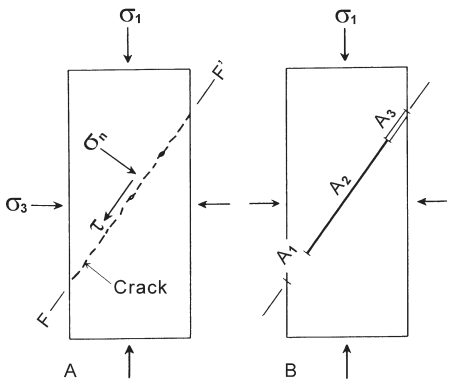

Figure 2.18. Simplified models of the cracked state along the eventual fault plane just before faulting.

Equations (2.2) and (2.5):

$$\tau_0 = \tau_1(\mathbf{A}_1/\mathbf{A}) \tag{2.6}$$

$$\mu_i = \mu(\mathbf{A}_2/\mathbf{A}) \tag{2.7}$$

These relations suggest a physical model for the cohesive strength (τ_0) and the coefficient of internal friction (μ_i).

According to the observation of microfracturing and the estimation from the strength versus pressure curve, the total area of closed crack surface ($\mathbf{A}_2$) just before the macroscopic fracture probably accounts for a large portion of the fault plane area ($\mathbf{A}$). Consequently, the coefficient of the internal friction (μ_i) is nearly equal to, although not the same as the coefficient of the external friction (μ). The cohesive strength (τ_0) is much smaller than the inherent shearing strength (τ_1) of the perfectly intact part. For example, $\mathbf{A}_2/\mathbf{A}$ and τ_0/τ_1 for Westerly granite were estimated from the strength versus pressure curve at 7/8 and 1/8, respectively, as will be mentioned in the later part. This is a model proposed by the author for explanation of the physical meaning of the Coulomb equation (Mogi, 1974).

Some investigators (e.g., Brace, 1964; Hoek, 1965) argued that there is good agreement between observed fracture strength of certain brittle rocks and prediction of the Coulomb criterion, taking the coefficient of internal friction 0.5–1.5; some of these values were, however, higher than the coefficients of sliding friction. Also, in experimental results under a wider pressure range, the strength versus pressure curves of some rocks are markedly concave towards the pressure axis at low confining pressure and near the brittle-ductile transition pressure. Therefore, the Coulomb criterion does not always hold for a wide pressure range, and the strength versus pressure curves are rather expressed by a power function (Matsushima, 1960; Murrell, 1965; Mogi, 1966; Byerlee, 1969).

In the following, it is shown that the pressure effect on the strength of brittle rocks is fundamentally expressed by the Coulomb theory, except for a low pressure region

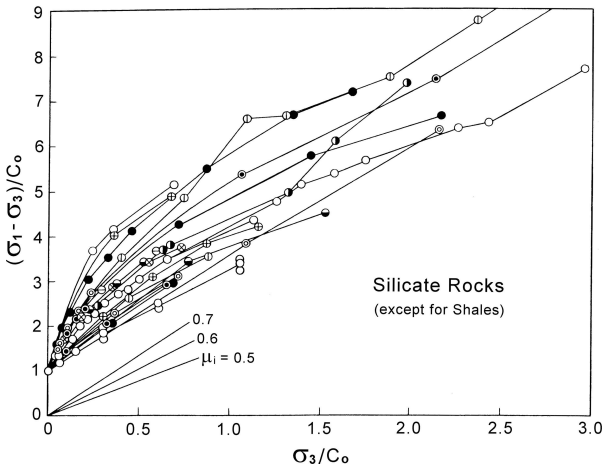

Figure 2.19. Compressive strength ($\sigma_1 - \sigma_3$) of silicate rocks, except for shales, against the confining pressure ($p = \sigma_2 = \sigma_3$), normalized by the uniaxial compressive strength C_0. μ_i: coefficient of internal friction.

in some rocks. Fig. 2.19 shows the strength versus pressure curves for silicate rocks (except for shales), based on published data until 1974 (Robertson, 1955; Handin and Hager, 1957; Matsushima, 1960; Brace, 1964; Mogi, 1964, 1965; Murrell, 1965; Raleigh and Paterson, 1965; Franklin and Hoek, 1970; Hoshino et al., 1972). These curves are limited to a very brittle region and the high-pressure region near the brittle-ductile transition pressure is not included. In this figure, the compressive strength and the confining pressure are normalized by dividing by the uniaxial compressive strength $\mathbf{C}_0$. In this coordinate system, the Coulomb equation is expressed by:

$$(\sigma_1 - \sigma_3)/\mathbf{C}_0 = 1 + \alpha\sigma_3/\mathbf{C}_0 \tag{2.8}$$

and the coefficient (α) is related with the coefficient of internal friction (μ_i) by:

$$\alpha = \left[(\mu_i^2 + 1)^{1/2} + \mu_i\right] / \left[(\mu_i^2 + 1)^{1/2} - \mu_i\right] - 1 \tag{2.9}$$

In Fig. 2.19, some of observed strength versus pressure curves are nearly linear and parallel to each other. Other curves, however, are concave toward the pressure axis in a low-pressure range and nearly linear in a higher pressure range. It is noticeable that the linear parts in both cases are roughly parallel to each other. The average slope (α) of the linear part of the strength versus pressure curves of these silicate rocks (except for shales) corresponds to a coefficient of internal friction of about 0.6. According to recent friction measurements, the coefficients of sliding friction of various silicate rocks are nearly equal to the above-mentioned coefficient of internal friction.

The coefficient of sliding friction of shales is significantly smaller than that of other silicate rocks (Maurer, 1965). If the Coulomb fracture criterion is applicable, it is expected that the slope (α) of the strength versus pressure curves of shales is smaller

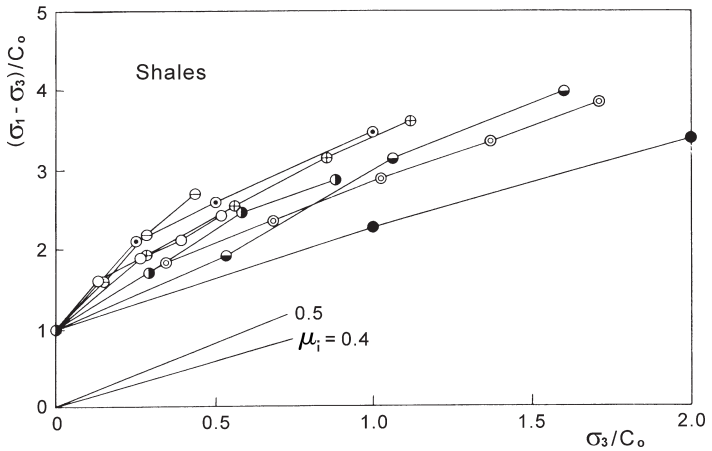

Figure 2.20. Compressive strength $(\sigma_1 - \sigma_3)$ of shales against the confining pressure $(p = \sigma_2 = \sigma_3)$, normalized by the uniaxial compressive strength C_0. μ_i: coefficient of internal friction.

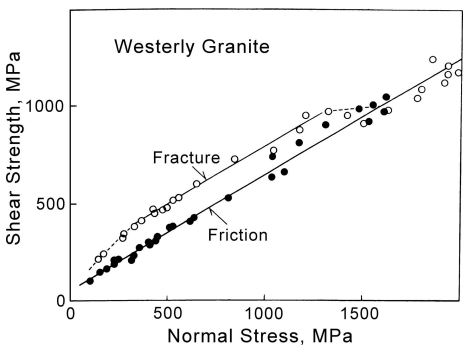

Figure 2.21. Shear stress versus normal stress at fracture (open circles) and friction on mated surfaces (solid circles) for Westerly granite. Data from Byerlee (1967).

than that of other silicate rocks. Fig. 2.20 shows that this is true. The coefficient of internal friction (about 0.4–0.5) obtained from the average slope of the linear part seems to be roughly equal to the coefficient of sliding friction (μ) obtained from Maurer's experimental result.

Figure 2.21 also supports the close relation between the fracture and friction curves. This figure was drawn by the author (Mogi, 1974) using the data from Byerlee (1967). In this figure, the following features can be pointed out: In Westerly granite, the shear stress versus normal pressure curve for fracture is nearly linear and parallel to the curve for sliding friction, except for the low-pressure region (∼400 MPa) and high-pressure region (∼1300 MPa). At the pressure of 1500 MPa and higher, the fracture curve agrees with the friction curve, and so deviation from the linear relation near

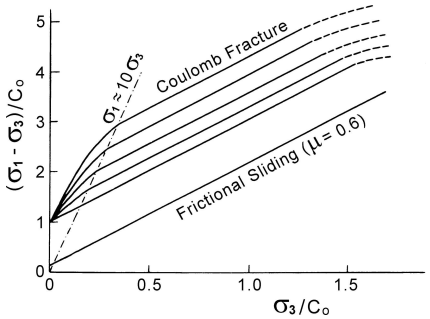

Figure 2.22. Typical strength versus pressure curves of rocks and the boundary line ($\sigma_1 \approx 10\sigma_3$) between the regions where the Coulomb criterion holds and where it does not hold.

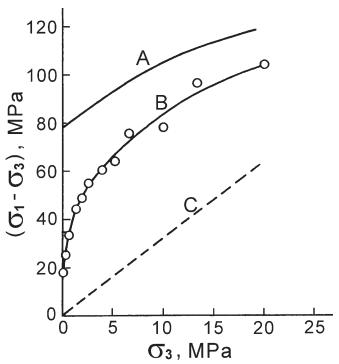

Figure 2.23. Compressive strength ($\sigma_1 - \sigma_3$) as a function of confining pressure ($p = \sigma_2 = \sigma_3$) for a marble. Curve A: original marble; curve B: marble with grain boundaries disintegrated by heating (after Rosengren and Jaeger, 1968); straight line C: frictional sliding ($\mu = 0.6$).

the normal pressure of 1500 MPa is attributed to the brittle-ductile transition process, which will be discussed later.

Thus, the Coulomb fracture criterion appears to apply to brittle fracture of many rocks, except for a low-pressure region and near the brittle-ductile transition pressure. Fig. 2.22 shows schematically the strength-pressure curves of various rocks. The curves of some rocks are concave toward the pressure axis in a low-pressure region. This high pressure-sensitivity of strength cannot be explained as a direct result of the pressure-sensitivity of the coefficient of sliding friction (Byerlee, 1967; Handin, 1969).

An interesting experimental result by Rosengren and Jaeger (1968) suggests a possible interpretation of high pressure-sensitivity of strength of rocks at low confining pressure. Their result is shown in Fig. 2.23. Curves A and B are the compressive fracture strength versus confining pressure curves for a virgin marble and for the same marble with grain boundaries disintegrated by heating, respectively. A curve for common sliding friction of marble is schematically shown by straight line C. It is noticeable

that curve B for the highly cracked marble is greatly different from curves A and C. This difference may be explained by the following two processes. The first is that the shear resistance for sliding on highly rough and interlocked surfaces, such as grain boundaries or joints, is much higher than that on smooth surfaces under low confining pressure. The second is that a number of open cracks at atmospheric pressure close with increase of confining pressure and so A_2 in Equation (2.5) or (2.7) increases, that is, the shear resistance of closed cracks increases markedly under confining pressure. Thus, it is reasonable that the high pressure-sensitivity of strength of the disintegrated marble is attributed to such effects of the cracked state. The strength versus pressure curves in the low pressure-region of silicate rocks shown in Figs. 2.19 and 2.20 can also be explained similarly by the state of cracks in rocks. For a high crack porosity, the pressure sensitivity of fracture strength is very high under low confining pressure and decreases with increasing confining pressure, and so the strength versus pressure curve tends to be concave toward the pressure axis at low confining pressure. In very compact rocks without appreciable pre-existing open cracks, the strength-pressure curve is nearly straight. In this case, the Coulomb fracture criterion is applicable. As mentioned above, in cases where there are appreciable open cracks, the strength versus pressure curve is concave toward the pressure axis and the Mohr criterion can be applied.

Recently, Savage, Byerlee and Lockner (1996) discussed this subject based on their careful measurements on fracture and friction of Westerly granite under confining pressure, from a similar standpoint as the author's. They obtained A_1/A, A_2/A and A_3/A as functions of the normal stress across that surface at failure and concluded that "the curvature in the strength-versus-normal-stress curve is explained in the Mogi model as being caused by changes in the relative proportions of cracked and intact areas on the incipient rupture surface, proportions which depend upon the prefailure loading trajectory." They state that what is called internal friction is simply a manifestation of ordinary friction. Moreover, the curvature of the Mohr failure envelope is a consequence of changes in the incipient rupture surface occupied by closed cracks, and that the portion depends in turn upon damage accumulated along the stress trajectory used to reach failure. These results of Mogi (1974) and Savage et al. (1996) showed that the Coulomb-Mohr criterion is not strictly empirical, but that it can be explained by a reasonable physical model.

2.2.c *Brittle-ductile transition*

With increase of confining pressure, ductility, which is defined as the ability to undergo large permanent deformation without fracture (Handin, 1966), increases markedly and a transition from the brittle to the ductile state takes place at some confining pressure. Fig. 2.24 shows typical stress-strain curves in the brittle, the transitional and the ductile state. Figs. 2.25 and 2.26 show the brittle-ductile behavior in the conventional triaxial compression test as functions of the confining pressure and compressive strength of silicate rocks and carbonate rocks, respectively (Mogi,

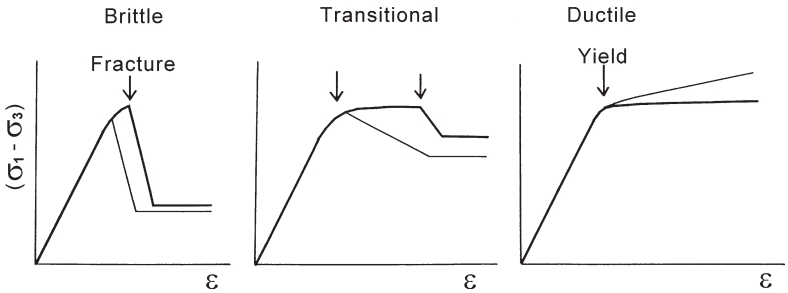

Figure 2.24. Typical stress-strain curves in the brittle, the transitional and the ductile state.

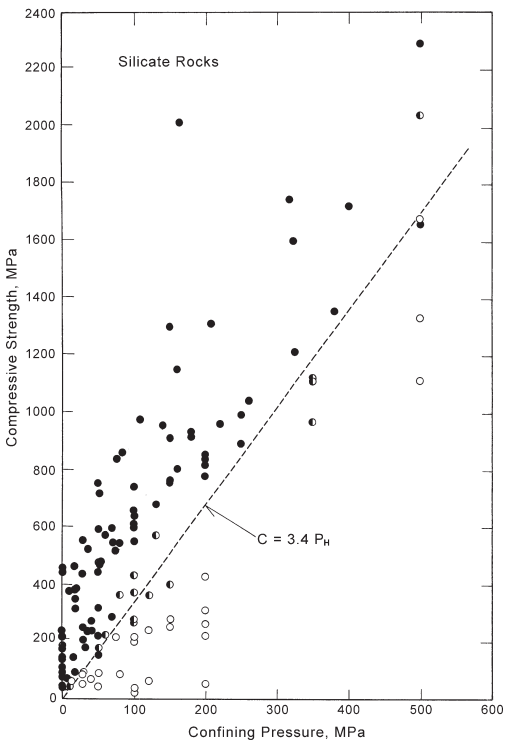

Figure 2.25. Failure behavior of silicate rocks at various strength and pressure. Dotted line: boundary between brittle region and ductile region; closed circle: brittle; semi-closed circle: transitional; open circle: ductile.

1966). In silicate rocks, the brittle state (closed circles) region and the ductile state (open circles) region is clearly divided by a straight line passing through the origin (Fig. 2.25). This boundary line is expressed by

$$(\sigma_1 - \sigma_3) = 3.4\sigma_3 \tag{2.10}$$

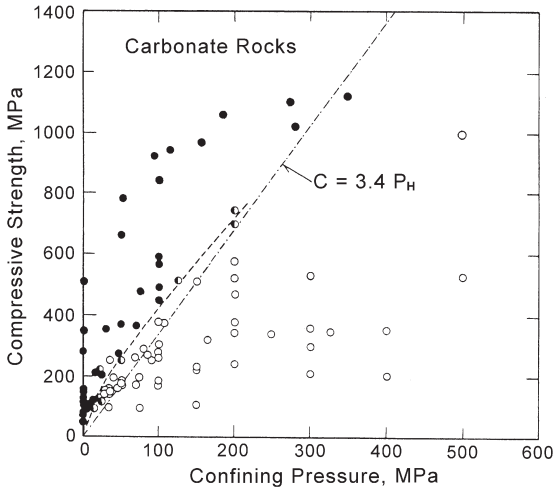

Figure 2.26. Failure behavior of carbonate rocks at various strength and pressure. Dotted line: boundary between brittle region and ductile region; closed circle: brittle; semi-closed circle: transitional; open circle: ductile.

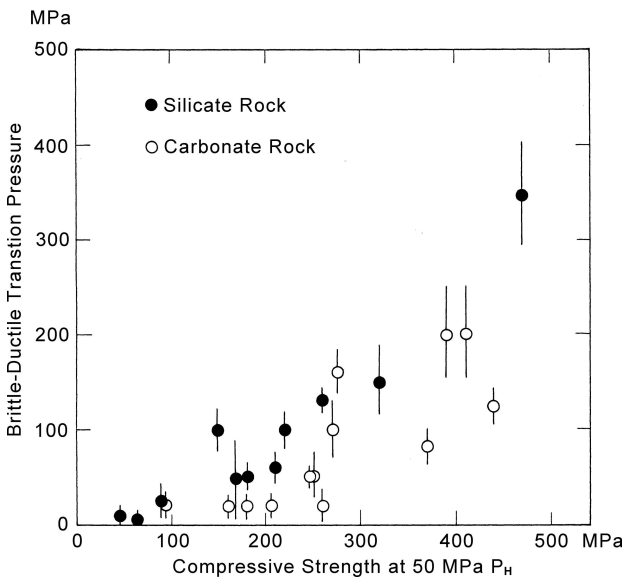

Figure 2.27. Relation between the brittle-ductile transition pressure and the compressive strength at 50 MPa confining pressure.

On the other hand, the boundary for carbonate rocks is somewhat different from that of silicate rock and clearly shifts to left side (Fig. 2.26). Fig. 2.27 shows the relation between the brittle-ductile transition pressure and the compressive strength at 50 MPa confining pressure in silicate rocks (closed circles) and carbonate rocks (open circles).

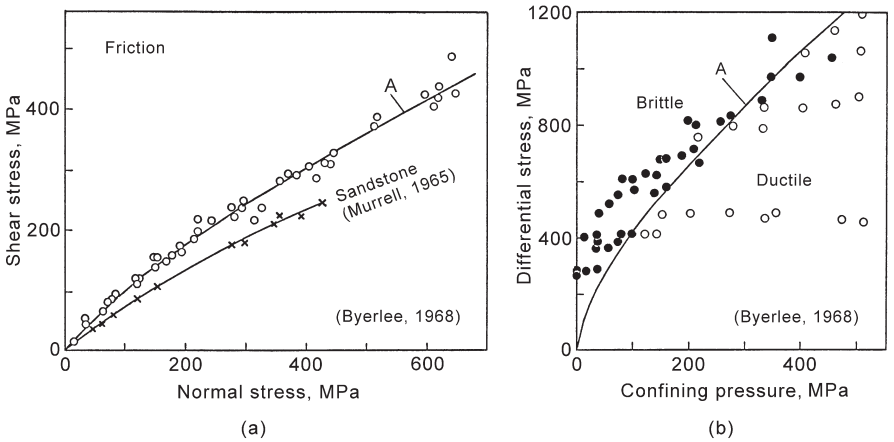

Figure 2.28. (a) Shear stress versus normal stress for friction. Circles: six rocks including Solnhofen limestone and Westerly granite (Byerlee, 1968); crosses: Darley Dale sandstone (Murrell, 1965). (b) Brittle-ductile behavior of five rocks as a function of confining pressure and differential stress at fracture or 5% strain if the specimen was ductile. Curve A is the boundary between brittle and ductile regions determined from friction data (Byerlee, 1968).

The brittle-ductile transition pressures of silicate rocks are appreciably higher than those of carbonate rocks. This difference between silicate rocks and carbonate rocks suggests that there are different mechanisms of the brittle-ductile transition in different rock types.

Orowan (1960) suggested that the stress drop characteristic of fracture does not occur at high pressure because frictional resistance on the fault surface becomes higher than the shearing strength of rock. This idea has been used as a possible explanation for the brittle-ductile transition by Maurer (1965), Mogi (1966), Byerlee (1968) and others. As mentioned above, the author (Mogi, 1966) pointed out that the brittle-ductile transition boundary in the strength versus pressure graphs is expressed by a nearly linear curve for various silicate rocks and the transition mechanism may be explained by Orowan's frictional hypothesis. The transition boundary in carbonate rocks is somewhat different from that in silicate rocks, this being attributed to a different transition mechanism. Byerlee (1968) discussed this problem based on his measurement of friction of rocks, and he argued that the brittle-ductile transition boundary is independent of rock type, and that Orowan's frictional hypothesis is applicable for both silicate and carbonate rocks. Fig. 2.28 shows the result by Byerlee (1968).

The author (Mogi, 1972) suggested that the frictional sliding hypothesis is applicable for the brittle-ductile transition process of rocks (noted as B-type) in which the permanent deformation in the post-yield region occurs by cataclastic flow or frictional sliding, but that it may not be applied to those of A-type, in which large permanent strain before fracture occurs by homogeneous plastic deformation. The typical stress-strain curves of A- and B-types are schematically shown in Figs. 2.29 and 2.30,

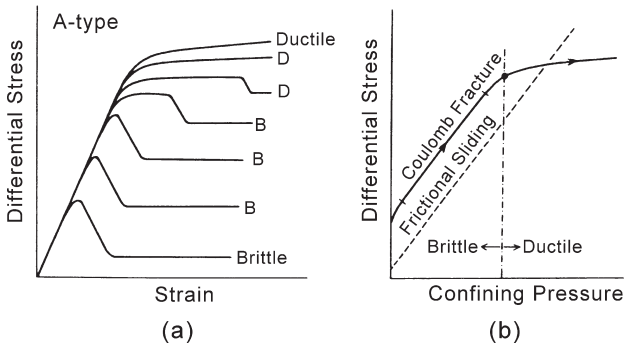

Figure 2.29. (a) Typical stress-strain curves of A-type rocks for different confining pressures. (b) Strength versus pressure curve and the failure behavior in A-type rocks.

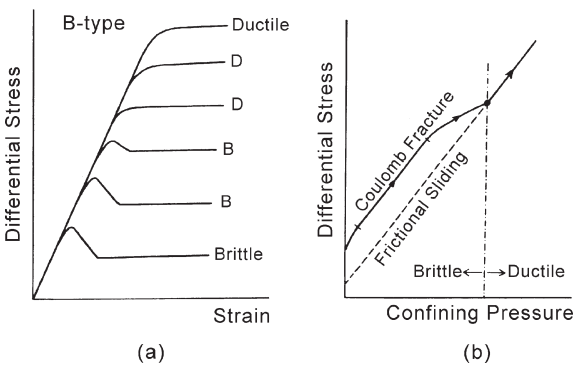

Figure 2.30. (a) Typical stress-strain curves of B-type rocks for different confining pressures. (b) Strength versus pressure curve and the failure behavior in B-type rocks.

respectively. Some carbonate rocks, particularly at high temperature, are A-type and silicate rocks are B-type.

Thus, the pressure dependence of strength of rocks near the transition pressure is different between A- and B-types. The strength versus pressure curves and their possible interpretations are summarized as follows.

1. *A-type*

The typical stress-strain curves of A-type rocks for different confining pressures and the strength versus pressure curve are shown in Fig. 2.29. In this case, faulting occurs after some permanent deformation, which increases with increasing pressure. The large permanent strain in the post-yield region before fracture occurs by homogeneous plastic deformation. The brittle-ductile transition may take place when the fracture strength is equal to the yield strength. In Fig. 2.29(b), the strength in a brittle region increases nearly linearly with increasing pressure and then the curve approaches the brittle-ductile transition boundary while at the same time decreasing its slope. The

decrease in the slope of curve near the transition pressure may be attributed to the gradual increase of local yielding due to heterogeneity (Mogi, 1966). At higher pressure, the yield strength approaches a constant value.

2. *B-type*

The typical stress-strain curves in this case are shown in Fig. 2.30 (a). The stress drop occurs just after the yield point and the permanent deformation in the post-yield region occurs by cataclastic flow or frictional sliding. The brittle-ductile transition pressure is the pressure at which the strength of rock at faulting is equal to the strength due to frictional resistance after faulting (Orowan, 1960). Figure 2.30 (b) shows the typical strength versus pressure curve. This curve is nearly parallel to the curve for frictional sliding on the fault surface, except for a low-pressure region. The slope of curve decreases gradually near the brittle-ductile transition pressure. This gradual decrease in the slope of curve is attributed to the increase of local fractures before faulting due to heterogeneity. That is, the area of the intact part ($\mathbf{A}_1$) in Equation (2.6) decreases gradually near the transition pressure, at which $\mathbf{A}_1$ becomes zero. At pressures higher than the transition pressure, the strength versus pressure curve agrees with the curve for frictional sliding, in which the strength increases linearly with increasing pressure. The strength versus pressure relation of Westerly granite shown in Fig. 2.21 is typical for the B-type.

Most rocks, however, behave in a manner intermediate between A- and B-types. Near the transition pressure, inelastic deformation just before and after yielding probably occurs both by fracturing and plastic deformation.

REFERENCES

Adams, F. D. and J. T. Nicolson. (1901). An experimental investigation into the flow of marble, Royal Soc. London Philos. Trans., Ser. A, **195**, 597–637.

Birch, F. (1960). The velocity of compressional waves in rocks to 10 kilobars, Part 1. J. Geophys. Res., **65**, 1083–1102.

Böker, R. (1915). Die Mechanik der bleibenden Formänderung in Kristallinisch aufgebauten Körpern. Ver. Dtsch. Ing. Mitt. Forsch., **175**, 1–51.

Brace, W. F. (1964). Brittle fracture of rocks. In: State of Stress in the Earth's Crust. Judd, W. R. (ed.). New York, Elsevier, 111–174.

Byerlee, J. D. (1967). Frictional characteristics of granite under high confining pressure. J. Geophys. Res., **72**, 3639–3648.

Byerlee, J. D. (1968). Brittle-ductile transition in rocks. J. Geophys. Res., **73**, 4741–4750.

Coulomb, C. A. (1773). Sur une application des régles maximis et minimis á quelques problémes de statique, relatifs á l'architecture. Acad. Sci. Paris Mem. Math. Phys., **7**, 343–382.

Franklin, J. A. and E. Hoek. (1970). Developments in triaxial testing technique. Rock Mech., **2**, 223–228.

Griggs, D. T. (1936). Deformation of rocks under confining pressure. J. Geol., **44**, 541–577.

Handin, J. (1966). Strength and ductility. In: Handbook of Physical Constants, Revised ed., Clark, S. P. (ed.), Geol. Soc. Am. Memoir, **97**, 223–289.
Handin J. (1969). On the Coulomb-Mohr failure criterion. J. Geophys. Res., **74**, 5343–5350.
Handin, J. and R. V. Hager. (1957). Experimental deformation of sedimentary rocks under confining pressure: tests at room temperature on dry samples. Bull. Am. Assoc. Petrol. Geol., **41**, 1–50.
Heard, H. C. (1960). Transition from brittle fracture to ductile flow in Solenhofen limestone as a function of temperature, confining pressure, and interstitial fluid pressure. In: Rock Deformation. Griggs, D., Handin, J. (eds.) Geol. Soc. Am., Memoir, **79**, 193–226.
Heard, H. C. (1963). Effect of large changes in strain rate in the experimental deformation of Yule marble. J. Geol., **71**, 162–195.
Hoshino, K., H. Koide, K. Inami, S. Iwamura and S. Mitsui. (1972). Mechanical properties of Japanese tertiary rocks under high confining pressure. Geol. Surv. Japan Rep., **244**, 1–200.
Jaeger, J. C. (1959). The frictional properties of joints in rock. Geofis. Pura Appl., **43**, 148–158.
Kármán, T. von (1911). Festigkeitsversuche unter allseitigem Druck. Z. Verein. Dtsch. Ing. **55**, 1749–1757.
Matsushima, S. (1960). On the deformation and fracture of granite under high confining pressure. Bull. Disaster Prevention Res. Inst. Kyoto Univ., **36**, 11–20.
Maurer, W. C. (1965). Shear failure of rock under compression. Soc. Pet. Eng. J., **5**, 167–176.
Mogi, K. (1964). Deformation and fracture of rocks under confining pressure (1) Compression tests on dry rock sample. Bull. Earthquake Res. Inst., Tokyo Univ., **42**, 491–514.
Mogi, K. (1965). Deformation and fracture of rocks under confining pressure (2), Elasticity and plasticity of some rocks. Bull. Earthquake Res. Inst., Tokyo Univ., **43**, 349–379.
Mogi, K. (1966a). Pressure dependence of rock strength and transition from brittle fracture to ductile flow. Bull. Earthquake Res. Inst., Tokyo Univ., **44**, 215–232.
Mogi, K. (1966b). Some precise measurements of fracture strength of rocks under uniform compressive stress. Felsmechanik und Ingenieurgeologie, **4**, 41–55.
Mogi, K. (1972). Fracture and flow of rocks. In: A. R. Ritsema (ed.), The Upper Mantle. Tectonophysics, **13** (1–4), 541–568.
Mogi, K. (1974). On the pressure dependence of strength of rocks and the Coulomb fracture criterion. Tectonophysics, **21**, 273–285.
Murrell, S. A. F. (1965). The effect of triaxial stress systems on the strength of rocks at atmospheric temperatures. Geophys. J. R. Astron. Soc., **10**, 231–281.
Orowan, E. (1960). Mechanism of seismic faulting. Geol. Soc. Am. Mem., **79**, 323–345.
Paterson, M. S. (1958). Experimental deformation and faulting in Wombeyan marble. Bull. Geol. Soc. Am., **69**, 465–476.
Paterson, M. S. (1978). Experimental Rock Deformation – The Brittle Field. Springer-Verlag, Berlin, pp. 254.
Raleigh, C. B. and M. S. Paterson. (1965). Experimental deformation of serpentinite and its tectonic implications. J. Geophys. Res., **70**, 3965–3985.
Robertson, E. C. (1955). Experimental study of the strength of rocks. Bull. Geol. Soc. Am., **66**, 1275–1314.
Rosengren, K. J. and J. C. Jaeger. (1968). The mechanical properties of an interlocked low-porosity aggregate. Geotechnique, **18**, 317–326.
Savage, J. C., J. D. Byerlee and D. A. Lockner. (1996). Is internal friction friction? Geophys. Res. Let., **23**, No. 5, 487–490.
Serdengecti, S. and G. D. Boozer. (1961). The effects of strain rate and temperature on the behavior of rocks subjected to triaxial compression. In: Proc. 4th Symp. Rock Mechanics. Hartman, H. L. (ed.). Penn. State Univ., Bull. Min. Ind. Exp. Sta., No. 76, 83–97.

Scholz, C. H. (1990). Mechanics of Earthquakes and Faulting. Cambridge Univ. Press, Cambridge, pp. 439.

Terzaghi, K. (1945). Stress conditions for the failure of saturated concrete and rock. Proc. Am. Soc. Test. Mater., **45**, 777–801.

Yamamoto, K., Y. Kuwahara, N. Kato and T. Hirasawa. (1990). Deformation rate analysis: A new method for *in situ* estimation from inelastic deformation of rock samples under uni-axial compressions. Tohoku Geophys. Journ., **33**, No. 2, 127–147.